INTERNATIONAL JOURNAL FOR NUMERICAL METHODS IN FLUIDS, VOL. 22, 283–296 (1996)

NUMERICAL MODELLING AND PARTICLE IMAGE VELOCIMETRY MEASUREMENT OF THE LAMINAR FLOW FIELD INDUCED BY AN ENCLOSED ROTATING DISC

M. ZHOU, C. P. GARNER AND M. REEVES

Department of Mechanical Engineering, Loughborough University of Technology, Loughborough, Leicestershire LE11 3TU, U.K.

SUMMARY

The fluid flow field within an enclosed cylindrical chamber with a rotating flat disc was calculated using a finite volume computational fluid dynamics (CFD) model and compared with particle image velocimetry (PIV) measurements. Two particular laminar cases near the Transitional flow regime were investigated: Reynolds number $Re = 2{\cdot}5 \times 10^4$, chamber aspect ratio $G\ (h/R_d) = 0{\cdot}2$ and $Re = 4{\cdot}2 \times 10^4$, $G\ (h/R_d) = 0{\cdot}217$. This enabled direct comparison with the numerical and experimental results reported by other researchers. The computational details and some major factors that affect the computed accuracy and convergence speed are also discussed in detail. PIV results containing some 4300 velocity vector points in each of seven planes for each case were obtained from the flow field parallel to the rotating disc. It was found that PIV results could be obtained in planes within the boundary layers as well as the core flow by careful use of a thin laser illumination sheet and correct choice of laser pulse separation. There was close agreement between numerical results, the present PIV measurements and other reported experimental and numerical results.

KEY WORDS: laminar flow; numerical modelling; particle image velocimetry measurement; rotating disc

1. INTRODUCTION

Fluid flows over the surfaces of rotating discs are of significant importance in turbomachinery design. Turbine discs, for example, required a suitable convective cooling flow to control disc temperatures and hence improve component performance and life. Many practical turbine disc systems can be idealized as a disc rotating in an infinite environment or in a chamber.

The work reported here concerns the computation and measurement of the flow field in a cylindrical disc chamber containing air. The flow is generated by a rotating disc within an enclosed stationary cylindrical shroud, which can be modelled in terms of the enclosed rotor–stator system as shown in Figure 1 (see Section 2). For the rotor-stator system, Daily and Nece[1] identified four possible flow regimes depending on the rotor Reynolds number Re and the height-to-radius aspect ratio G, namely laminar or turbulent flow with merged or separated boundary layers on the rotor and stator. The present work corresponds to the regime of laminar flow with separated boundary layers. Previous numerical efforts in studying this type of flow based on the solution of the Navier–Stokes equations have been performed by a number of researchers.[2–6] However, for the laminar cases with disc rotational Reynolds number Re (near or in the transitional flow regime), convergence difficulties with the numerical

CCC 0271–2091/96/040283–14

Received October 1994

solution have been found by Nakata *et al.*,[2] Chew[3] and Bar-Yoseph *et al.*[4] A number of experimental studies pertinent to this type of flow have also been reported. Daily and Nece,[1] for example, used a modified Pitot-static tube to measure the velocities and Dijkstra and Van Heijst[5] obtained experimental results based on stereophotography of small tracer particles. Laser–Doppler anemometry (LDA) measurements were also reported by Sambo[6] and Riahi and Hill.[8]

In the present study, two cases of laminar flow near or in the transitional flow regime were modelled using the computational fluid dynamics (CFD) code FLUENT.[9] The grid dependence was examined and the major factors that affect the convergence speed, such as the choice of underrelaxation factor and initial estimates, are discussed in detail. The two cases were chosen to be the same as in the numerical work reported by Nakata *et al.*[2] and the experimental study, obtained from a liquid flow rig, by Daily and Nece[1] respectively.

The flow fields for these specific cases were also studied experimentally by the present authors using the particle image velocimetry (PIV) technique.[10,11] This technique has undergone rapid development in recent years and has been used in many studies of fluid flow. PIV provides instantaneous two-dimensional velocity vector maps from a chosen plane in the flow and hence yields many useful data to validate the computational results. The accuracy of PIV has been shown to be within the range of several per cent to a few tenths of a per cent and measurements can be made at small length scales between several millimetres and several tenths of a millimetre.[12] These features are considered suitable to make PIV useful for quantitative evaluation of the present flow.

It is important to note that the numerical results were assessed in a number of ways, namely

(a) grid dependence,
(b) direct comparison with numerical results reported by other investigators,
(c) direct comparison with experimental results reported by other investigators,
(d) direct comparison with our experimental results obtained with the present PIV analysis.

2. NUMERICAL PREDICTION

2.1. *Governing Equations and Solution Procedure*

For the present study cases the flow can be assumed to be laminar, steady and axisymmetric. Additionally, constant fluid properties were assumed; therefore the three momentum equations and the continuity equation can be written as

$$\frac{1}{r}\frac{\partial(\rho r u^2)}{\partial r}+\frac{\partial(\rho u w)}{\partial z}=-\frac{\partial p}{\partial r}+\frac{1}{r}\frac{\partial}{\partial r}\left(\mu r\frac{\partial u}{\partial r}\right)+\frac{\partial}{\partial z}\left(\mu\frac{\partial u}{\partial z}\right)-\mu\frac{u}{r^2}+\frac{\rho v^2}{r}, \tag{1}$$

$$\frac{1}{r}\frac{\partial(\rho r u v)}{\partial r}+\frac{\partial(\rho v w)}{\partial z}=\frac{1}{r}\frac{\partial}{\partial r}\left(\mu r\frac{\partial v}{\partial r}\right)+\frac{\partial}{\partial z}\left(\mu\frac{\partial v}{\partial z}\right)-\mu\frac{v}{r^2}-\frac{\rho u v}{r}, \tag{2}$$

$$\frac{1}{r}\frac{\partial(\rho r u w)}{\partial r}+\frac{\partial(\rho w^2)}{\partial z}=-\frac{\partial p}{\partial z}+\frac{1}{r}\frac{\partial}{\partial r}\left(\mu r\frac{\partial w}{\partial r}\right)+\frac{\partial}{\partial z}\left(\mu\frac{\partial w}{\partial z}\right), \tag{3}$$

$$\frac{1}{r}\frac{\partial(\rho r u)}{\partial r}+\frac{\partial(\rho w)}{\partial z}=0, \tag{4}$$

with the following boundary conditions:

(i) at the surface of the rotating disc: $z=0$; $u=0$, $v=r\Omega$, $w=0$;
(ii) at the stationary surface facing the rotating disc: $z=h$; $u=v=w=0$;
(iii) at the stationary cylindrical shroud: $r=R_d$; $u=v=w=0$.

The FLUENT code uses a finite volume numerical procedure to solve the full Navier–Stokes equations. The numerical technique employed in FLUENT involves the subdivision of the domain of interest into a finite number of control volumes or cells. The partial differential equations are discretized over these cells to obtain a set of simultaneous algebraic equations. All the dependent variables, with the exception of velocity components, are calculated and stored at the nodal points (i.e. the grid intersection points) which these cells encompass. A staggered grid is employed for the storage and calculation of the velocity components on the cell boundaries.

The iterative solution based on the SIMPLE algorithm is described in Reference 13. At each iteration of its solution algorithm a normalized residual $\bar{R}$ is reported for each equation that has been solved. These residuals provide a measure of the degree to which each equation is satisfied through the flow field. The normalized residual $\bar{R}$ in generalized form is defined as

$$\bar{R} = \frac{\sum |a_p\phi_p - \sum a_k\phi_k - S_u|}{\sum a_p\phi_p}, \tag{5}$$

where ϕ may stand for any of the velocity components or the pressure, $a_p\phi_p$ represent the calculated values at node p, $\sum a_k\phi_k$ represents the summation over the adjacent nodes surrounding the finite difference node p, and S_u donates the source term.

As Reference 9 recommends, a solution can be considered to have converged when the normalized residuals are of order 1×10^{-3} (except the enthalpy residual which should be about 1×10^{-6}). To ensure a greater accuracy, in the present study a value of $0{\cdot}5 \times 10^{-3}$ was chosen as the maximum normalized residual to determine whether or not the solution has converged.

2.2. Computational Details

The geometric configuration of the disc chamber is shown schematically in Figure 1. The radius of the disc is $R_d = 40$ mm and the gap between the disc and the cylindrical shroud is $d = 0{\cdot}125$ mm, which gives $d/R_d = 0{\cdot}003125$. Since d is very small and two rubber sealing rings were placed under the disc to ensure that in the steady state there was no flow through the gap, any effects of this gap have been neglected as Reference 7 allows. The height h can be adjusted to obtain the required aspect ratio G. In order to compare the results of Nakata *et al.*[2] and Daily and Nece[1] directly, two laminar flow cases were computed.

Case 1. Laminar flow, $Re = 2{\cdot}5 \times 10^4$, $G = 0{\cdot}2$—the same as in the numerical investigation of Nakata *et al.*[2]

Case 2. Laminar flow, $Re = 4{\cdot}2 \times 10^4$, $G = 0{\cdot}217$—the same as in the experimental investigation of Daily and Nece.[1]

These two cases are both near or in the transitional flow regime.[2] The reference density and viscosity of the air were taken as those appropriate to air at $P_o = 101{\cdot}3$ kPa and $T_o = 288$ K, namely $\rho = 1{\cdot}226$ kg m^{-3} and $\mu = 1{\cdot}786 \times 10^{-5}$ kg m^{-1}s^{-1}. Some important computational details are now described.

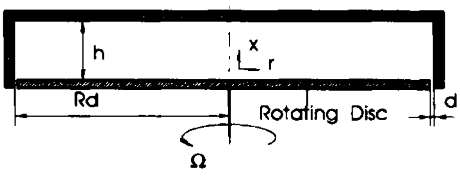

Figure 1. Configuration of disc chamber

2.2.1. Grid specification and grid dependence. A grid dependence study was conducted. Taking into account the axial symmetry of the disc chamber geometry and flow field, a solution domain consisting of a 1° sector grid with four cells in the circumferential direction was used as shown in Figure 2. For all computations, non-uniform grid points were generated in the axial–radial plane of the domain to make the computation more efficient. Smooth expansions and contractions in grid spacing are used to obtain sufficient resolution in the boundary layers, i.e. the grid points near the disc and stationary shroud surfaces (boundary layers) were set closely and the grid points near the centreline ($r=0$) and the mid-plane of the axial clearance were set sparsely.

It was found that the numerical accuracy was sensitive to the grid specification in the axial–radial plane, especially with regard to the number of cells in the axial direction. Significant effort was made to examine this effect on the numerical results. A number of computations using different grid point distributions in the axial–radial plane for Case 1 were carried out as shown in Table I. The numbers of cells in the axial direction were chosen as 22, 42, 62 and 82 and the corresponding cell numbers in the radial direction were selected as 22, 42, 57 and 75. For the grid choice of 22 × 22 × 4 (axial, radial and tangential directions respectively) and 42 × 42 × 4 an expansion factor of 1·1 was used to set the grid points from the disc surface to the mid-plane and an expansion factor of 0·9 was used to compress the grid points from the mid-plane to the top of the chamber. For the choice of 62 × 57 × 4 and 82 × 75 × 4 cell distributions, expansion factors of 1·05 and 0·95 were used.

The comparison of the ratio of the angular velocity of the fluid core to that of the rotating disc, $K=\beta/\Omega$ at $r/R_d=0{\cdot}8$, for the different choices of grid specification of Case 1 is shown in Table I. It is clear that the difference between choices 3 and 4 is less than 1%. Hence choice 3, i.e. the grid specification with 62 points in the axial direction and 57 points in the radial direction, was considered to be adequate for grid independence and was employed in the present computation for both cases.

2.2.2. Convergence speeding. Convergence can be slow owing to a number of factors such as a large number of computational cells and the complexity of the flow physics. Convergence difficulties were experienced in cases with high rotational Reynolds numbers for laminar flow, especially the laminar flow near or in the transitional regime as reported elsewhere.[2–4] The present cases at $Re=2{\cdot}5\times10^4$ and $4{\cdot}2\times10^4$ also encountered convergence difficulties. This is because the present flow is very near the transitional regime.[2] Chew[3] pointed out that the slow solution convergence is related to instabilities in the physical flow at this condition. Some important factors that affect the speed of convergence in the present study are described now. These include the underrelaxation factor, the initial estimate and the sweep direction of the solution procedure.

The underrelaxation factor α controls how much the variables are allowed to change at each iteration. The behaviour of the solution is sensitive to this factor, especially when the disc Reynolds number is high. An attempt to calculate the flow of Case 1 with a lower disc Reynolds number of $1{\cdot}25\times10^4$ was made; α was selected to be 0·5 for velocity components, 0·8 for pressure correction and 0·4 for other variables and approximately 800 iterations were necessary to obtain a converged solution. With an increase in Reynolds number to $2{\cdot}5\times10^4$ the solution began to oscillate and

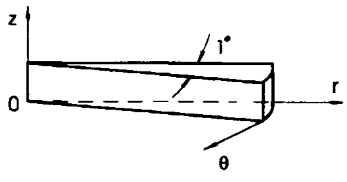

Figure 2. Solution domain

Table I. Effect of grid number on computational results

Choice	Number of grid cells (axial × radial × tangential = total)	Angular velocity ratio $K=\beta/\Omega$
1	22 × 22 × 4 = 1936	0·452
2	42 × 42 × 4 = 7056	0·408
3	62 × 57 × 4 = 14136	0·388
4	82 × 75 × 4 = 24600	0·385

converge slowly and more than 6000 iterations were required, even with the pressure underrelaxation factor $\alpha = 0{\cdot}5$ (α for pressure is more sensitive to solution convergence than the others).

Theoretically, whether the initial estimate is given or not and what value it takes will have no effect on the convergence ultimately. However, supplying a good initial velocity guess is a very useful approach to accelerate convergence. For computation of the present cases, initial core velocities corresponding to $K = 0{\cdot}37$ for Case 1 and $K = 0{\cdot}35$ for Case 2 were supplied at five grid points of the solution domain at $r/R_d = 0{\cdot}8$ and $0{\cdot}765$ respectively. Combined with choosing suitable underrelaxation factors ($\alpha = 0{\cdot}7$ for pressure correction and $\alpha = 0{\cdot}4$ for the others), the converged solution was obtained satisfactorily.

Another approach that may accelerate convergence is to choose the correct sweep direction of the solution procedure. The 'default' sweep direction is the radial direction. This means that the equations are solved simultaneously at each successive column of cells (or sweep in the radial direction) by marching in the predominant flow direction (i.e. the circumferential direction). Since the boundary conditions in the axial direction (including the velocity on the surface of the disc) are of particular importance to the solution, the axial direction was chosen as the sweep direction and the convergence speed was therefore accelerated by this alteration.

2.3. *Computational Results*

Since the two cases are similar, only the computational results of Case 1 are presented in detail here. The computed flow structure of Case 1 is illustrated by the streamline plot in Figure 3, while the velocity vector map in the axial–radial plane is shown in Figure 4. These figures indicate that the flow consists of a well-developed fluid core and separate boundary layers near the top and bottom of the disc chamber. Fluid mass flows radially outwards in the layer on the rotor owing to centrifugal effects and travels radially inwards next to the stator. The entire flow forms a single vortex which recirculates with a centre close to the cylindrical shroud. Details of the local velocity distributions are shown in Figure 5. The radial velocity (Figure 5(a)) in the fluid core is near zero and the circumferential velocity (Figure 5(b)) is nearly constant. The axial velocity (Figure 5(c)) is also nearly constant in the core and very small compared with the circumferential velocity.

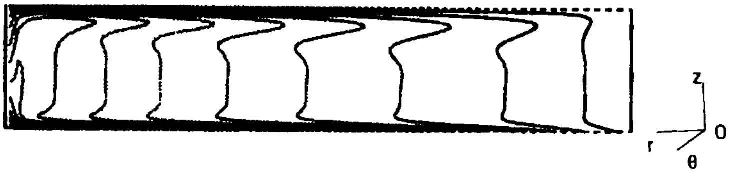

Figure 3. Calculated streamline of Case 1 in axial–radial plane

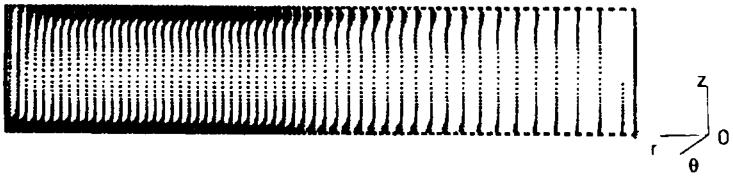

Figure 4. Predicted velocity distribution of Case 1 in axial–radial plane

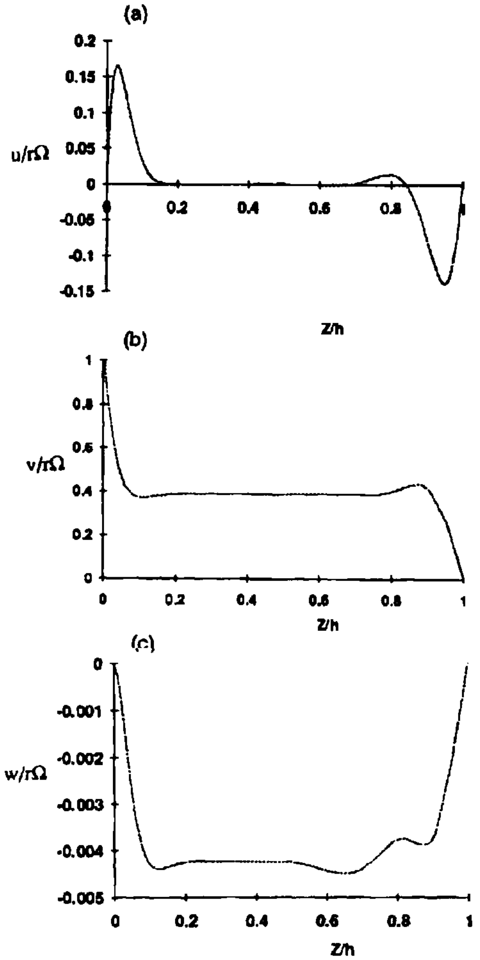

Figure 5. Computation results of Case 1 at $Re=2{\cdot}5\times 10^4$, $G=0{\cdot}2$, $r/R_d=0{\cdot}8$: (a) radial velocity; (b) circumferential velocity; (c) axial velocity

3. PIV MEASUREMENTS OF THE FLOW FIELD

Particle image velocimetry (PIV) measurements of the flow field were conducted for comparison with the numerical results. With PIV, velocity measurements are made by seeding the flow and taking a photograph of a laser light sheet which is formed in the plane of interest. The laser light source is double pulsed so that two images of each seeding particle are recorded by the camera. The subsequent photographic transparency is pointwise analysed (interrogated) by autocorrelating small regions containing a cluster of approximately 10 particles to yield the mean particle displacement between laser pulses and hence the mean velocity in each region of the flow. The experimental details are now described.

3.1. Experimental Arrangement and Techniques

Experiments were carried out using the arrangement shown schematically in Figure 6. The laser used for illumination was a pulsed ruby laser which can supply double pulses of 694 nm (deep red) light with energies of order 1 J and Q-switched pulse duration of around 50 ns. The pulse separation can be set in the range of 1 μs to 1 ms. The laser beam is formed into a sheet by passing it through a positive cylindrical lens and a negative spherical lens. The light sheet enters and leaves the disc chamber via an acrylic periphery and the PIV images were recorded with a camera viewing perpendicularly to the laser sheet through the top window of the disc chamber. The disc chamber is mounted on a translation stage which can be moved perpendicularly to the camera. Its movement was monitored by a microclock with a minimum division of 0·001 inch (25·4 μm) so that the measuring plane along the axial direction can be selected with good precision. A 35 mm camera at an aperture ratio of 5·6 was used to record the particle images in the flow field at a magnification of 0·5. Owing to the symmetry of the flow, only a quadrant of the whole circular flow field was recorded. This permitted measurements at a higher spatial resolution without exceeding the resolution of the photographic film. The film type chosen for this work was Kodak Technical Pan 2415, developed with D-19 to give a speed of around 100 ASA at a resolution of approximately 200 line pairs per millimetre.

The flow was seeded with 0·5–2·0 μm olive oil particles which were generated by passing air at approximately 70 kPa gauge pressure through a bath of olive oil. The resulting particle mist was passed through a simple separator to remove larger droplets. The particle density can be controlled by altering the air supply pressure. Prior to each measurement the disc chamber was filled with a sufficient quantity of seed. The chamber was then isolated from the seeding flow by closing the inlet and outlet valves.

Interrogation of the recorded PIV images was performed by two-dimensional digital autocorrelation analysis using an AEA Harwell PIV System.[14] The system consists of a 33 MHz 386 PC, a computer-controlled translation stage on which the PIV transparency is mounted, a video macro lens and extension tubes for viewing a magnified portion of the image, and a PC-based framestore and array processor for capturing the images and performing the two-dimensional fast Fourier transforms (FFTs) required to generate the autocorrelation. For the present image analysis an FFT resolution size of 256 × 256 pixels was chosen. The interrogation region size was $0{\cdot}54 \times 0{\cdot}54\ \mathrm{mm}^2$ on film, corresponding to a $1{\cdot}08 \times 1{\cdot}08\ \mathrm{mm}^2$ region in the flow field.

The transparency was interrogated on a regular square grid with 50% overlap between neighbouring

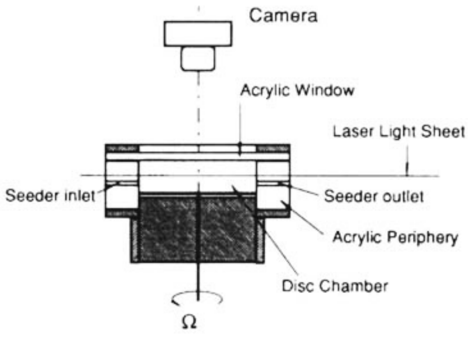

Figure 6. Experimental arrangement for PIV measurements

regions. The autocorrelation plane for each region consists of a large central peak and a number of non-central potential signal peaks. The co-ordinates of the centroids of the three highest non-central peaks are stored in rank order of height, the highest peak being the most likely true signal peak. The displacement of the true signal peak from the centre of the autocorrelation plane is a measure of the mean particle displacement and hence the velocity in that region. In cases where the highest peak gives a deviant velocity vector, this can be replaced by the second or third candidate. Where neither is appropriate, the vector can be deleted and replaced with an interpolated value if required. This process of validation can be performed automatically using flow continuity criteria.

3.2. Illuminating Laser Sheet

In PIV experiments it is important to match the properties of the illuminating laser sheet to the flow being investigated. In highly three-dimensional flows, out-of-plane velocity components cause particle pairs to be lost from the light sheet plane if the light sheet is too thin. Also, if large out-of-plane velocity gradients exist, such as in boundary layers where the measurement plane is parallel to the boundary, the resulting spread of velocities within each interrogation region can be prohibitively large if the light sheet is too thick. This can lead to significant biasing of the mean velocity determined by autocorrelation.[15] In typical PIV experiments there is therefore a compromise between tolerance to out-of-plane velocities and out-of-plane velocity gradients.

For the present case the flow is known to be laminar with negligible out-of-plane velocity components. This allows the sheet thickness to be minimized such that the large out-of-plane velocity gradients within the boundary layers can be accommodated, permitting comparisons of PIV measurements with CFD predictions of velocity distributions within 1 mm of the surfaces of the rotating and fixed discs.

The lay-out of the sheet-forming optics is shown in Figure 7(a). A positive cylindrical lens of focal

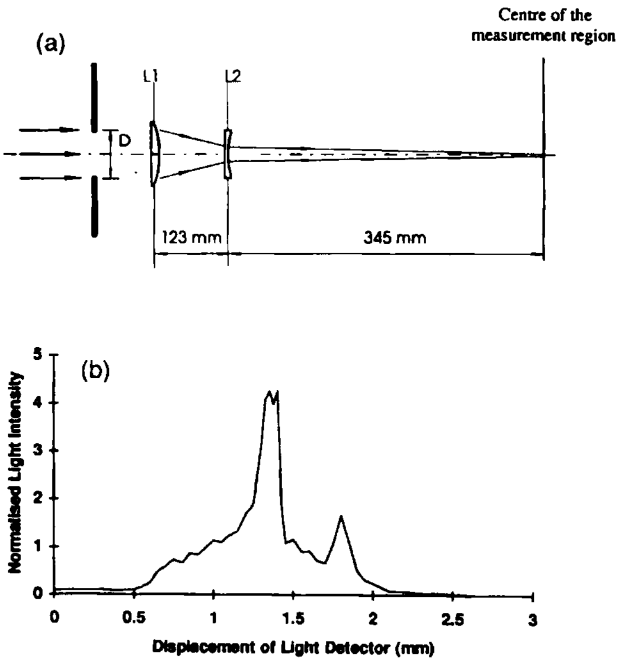

Figure 7. Formation of illumination laser sheet: (a) optical arrangement; (b) light sheet profile

length 150 mm and a negative spherical lens of focal length − 50 mm are arranged such that the focal waist of the light sheet falls at the centre of the measurement region. The thickness of the light sheet waist was measured by traversing a pinhole and photodetector through the sheet and normalizing the resulting voltage output to the laser pulse energy as measured by an energy monitor placed at the laser output. The resulting laser sheet profile is shown in Figure 7(b), the FWHM sheet width being approximately 0·2 mm.

3.3. *Experimental Results*

Seven different axial planes corresponding to $z/h = 0{\cdot}05$, 0·1, 0·3, 0·5 (the mid-plane), 0·7, 0·9 and 0·95 were measured for each of Cases 1 and 2. Owing to the axial symmetry of the flow field, PIV images of a quarter of the whole field were recorded and interrogated to illustrate the overall flow structure. An example of an interrogated and post-processed (validated) velocity vector map resulting from the PIV image in the mid-plane of Case 1 is shown in Figure 8. Every image (a quarter of the whole flow field) contains approximately 4300 interrogation regions and hence yields 4300 velocity vector points. However, the raw (unvalidated) vector map resulting from interrogation of PIV images may have a number of erroneous vectors for several reasons, including excessively large or small particle displacements, out-of-plane velocity components causing one of the particle image pairs to move out of the illumination light sheet, high velocity gradients and random noise on the film.[16] Therefore a post-interrogation refinement procedure was performed to correct the significant erroneous velocities that were different from their neighbours by more than a predetermined bound of acceptability (i.e. approximately 30% difference in magnitude and 45° in direction). In this example, fewer than 15% of the interrogation data were considered invalid and were corrected.

For direct quantitative comparison with other computational and experimental results, only the individual circumferential velocities lying at specific radii $r/R_d = 0{\cdot}8$ (Case 1) and $r/R_d = 0{\cdot}765$ (Case

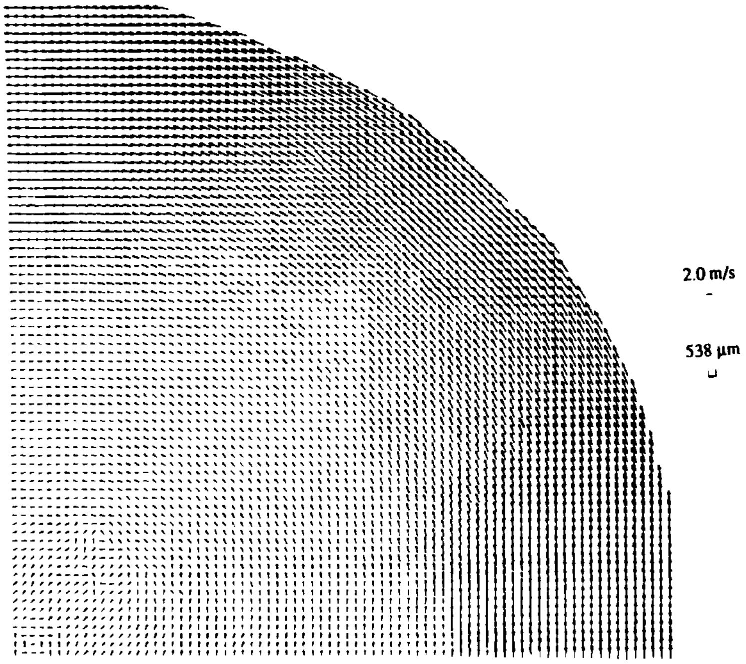

Figure 8. Validated PIV velocity data of Case 1 at mid-plane

2) were actually required. The extraction of particular velocities of interest is shown schematically in Figure 9. Although each PIV transparency contains all the spatial information, processing efficiencies could be achieved by only interrogating regions at these required radii.

Two PIV transparencies were recorded for each plane and 30 discrete interrogation regions of size 0·54 × 0·54 mm^2 were interrogated for each transparency at the required radius. Therefore a total of 60 velocity vectors were obtained at the required radius in every plane. These discrete interrogation regions were selected manually and the vectors that showed significant visual discontinuity from their

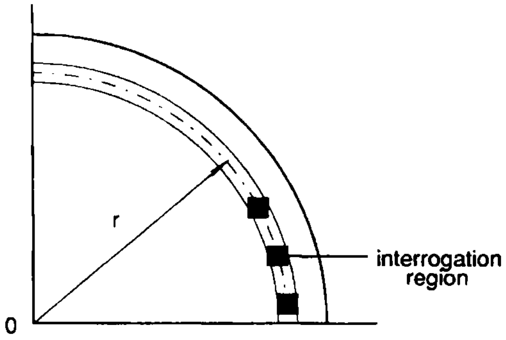

Figure 9. Schematic illustration of velocity extraction at a particular radius *r* from PIV images

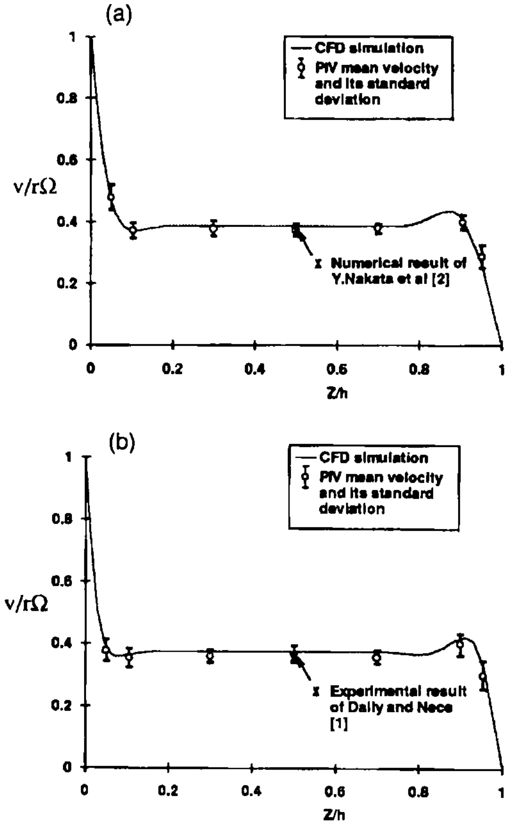

Figure 10. Comparison between numerical and experimental results: (a) case 1; (b) case 2

neighbours were ignored. From these 60 points an ensemble-averaged mean velocity and its standard deviation were calculated as shown in Figure 10, thereby giving a measure of the random error of PIV results.

4. COMPARISON AND DISCUSSION OF RESULTS

4.1. Comparison of Results

The comparison of the ratio of the angular velocity of the fluid core to that of the rotating disc, $K=\beta/\Omega$, between the computed results, the PIV measurements and the results conducted by other investigators is shown in Figure 10. All the processed PIV results of two cases are shown, i.e. the mean velocities and their standard deviations at different planes along the axial clearance of the disc chamber. The results compare quite favourably. The quantitative comparison of K from all the results is presented in Table II. Again, close agreement between the results is found.

4.2. Discussion

The PIV measurements have been made to obtain planar velocity maps in the present work. This aids understanding of the flow field and provides obvious comparison with other results. PIV has also been used reliably in other complex and difficult fluid mechanics experiments to obtain information that was unattainable by other experimental methods.[12] However, some fundamental limitations exist in the technique. These include out-of-plane motion, velocity dynamic range, velocity gradients and directional ambiguity. The major limitations relevant to the present work are now discussed.

4.2.1. PIV measurements at boundary layers. The CFD predictions of circumferential velocity profiles exhibit steep gradients close to the boundaries (Figure 10). It has been shown that the accuracy of velocity determination by spatial autocorrelation is profoundly affected by velocity gradients.[15] Expressed simply, velocity gradients give rise to a variety of individual particle pair displacement within a single interrogration region. The effect of weak velocity gradients is to broaden the signal peaks in the autocorrelation plane and introduce a measurement bias towards velocities lower than the true mean velocities. This bias is known as 'velocity gradient bias'. At higher velocity gradients, sufficient to cause a scatter in diplacements of the order of the individual particle image diameter, the signal peak either broadens or splinters into a number of individual peaks. In this case the peak closest to zero velocity is usually the largest and is therefore selected as the most likely displacement vector; hence a very large detection bias of the order of the half-spread in the particle velocity within a region can result.

When performing measurements in boundary layers or other flow regimes exhibiting high velocity gradients, it is therefore important to minimize these bias effects and estimate their magnitudes. In the present work the in-plane velocity gradients in the core flow are negligible compared with the out-of-plane velocity gradients in the boundary layers and only the effects of the latter need be discussed.

Table II. Comparison of angular velocity ratio K at mid-plane

	$K=\beta/\Omega$	
Results	Case 1	Case 2
Present computational results	0·388	0·375
Present PIV results	0·372	0·366
Numerical results of Nataka *et al.*[2]	0·377	—
Experimental results of Daily and Nece[1]	—	0·36

Keane and Adrian[15] have shown that the magnitude of the velocity bias towards zero velocity as a proportion of the true mean velocity is approximated by

$$B_{\mathrm{f}} = M\Delta u \Delta t / d_{\mathrm{I}}, \tag{6}$$

where B_{f} is the fractional bias, M is the camera magnification, Δt is the pulse separation, d_{I} is the interrogation region size in the plane of the light sheet and Δu is the maximum excursion of the velocity from the mean within the interrogation cell. For out-of-plane velocity gradients the value of Δu is given by

$$\Delta u = \frac{\Delta z}{2} \frac{\mathrm{d}u}{\mathrm{d}z}, \tag{7}$$

where Δz is the laser sheet thickness and $\mathrm{d}u/\mathrm{d}z$ is the velocity gradient across the sheet thickness. Combining these two equations gives the final estimate of the velocity gradient bias within the boundary layer as

$$B_{\mathrm{f}} = \frac{M \Delta t \Delta z}{2 d_{\mathrm{I}}} \frac{\mathrm{d}u}{\mathrm{d}z}. \tag{8}$$

To minimize the gradient bias for a given velocity gradient, it is therefore necessary to minimize the pulse separation to permit relatively small particle displacements compared with the interrogation region dimension, as well as to minimize the laser sheet thickness.

In the present work the velocity gradient corresponding to the first PIV measurement point in Figure 10(a) is estimated from the CFD prediction curve to be approximately 3000 s^{-1}. Inserting appropriate values for the experimental parameters in equation (8), we have $M = 0{\cdot}5$, $\Delta t = 40 \times 10^{-6}$ s, $\Delta z = 0{\cdot}2 \times 10^{-3}$ m, $\mathrm{d}u/\mathrm{d}z = 3000\ \mathrm{s}^{-1}$ and $d_{\mathrm{I}} = 0{\cdot}54 \times 10^{-3}$ m, giving a velocity gradient bias of approximately 1·1%.

Since the experimental error is of the same order, the velocity bias can therefore be tolerated. It should be pointed out that this low bias was achieved by use of an extremely thin light sheet and a small pulse separation which permitted particle image separations of only a few particle imaging diameters. The nature of the flow is predominantly two-dimensional and in the plane of the light sheet. In more general flows the sheet cannot be made thin without significant loss of particle image pairs due to the out-of-plane velocity component. Also, since measurements were only extracted at a single radial distance for each measurement plane, the required velocity dynamic range was limited and the laser pulse separation could be optimized at a low value. In a general PIV experiment the pulse separation would have to be larger to cope with a significant range of velocities in a flow and this would increase the measurement bias in proportion to the pulse separation.

4.2.2. Directional ambiguity. When a conventional PIV image is viewed, the first and second particle images are identical. Therefore, since it is not known which came first, a 180° directional ambiguity exists. Several approaches have been proposed or applied for resolving this problem.[17] However, in the present study, since the flow is known to be laminar and symmetrical, the directional ambiguity problem was not important and therefore not addressed.

5. CONCLUSIONS

Tests with the numerical finite volume CFD model showed that grid-independent numerical results could be achieved. For the present laminar flow region with high rotational Reynolds numbers, convergence could be accelerated and obtained by correct choice of underrelaxation factor and by providing good initial velocity estimates.

Quantitative comparison of CFD analysis with PIV measurements and numerical and experimental results of other researchers was made. There was close agreement. Both the results from the present numerical model and the PIV measurements revealed a flow field consistent with other reported work. Boundary layers formed on the disc and stationary shroud surfaces were separated by a rotating fluid core in the central region of the cavity.

It was demonstrated that favourable PIV measurements could be made within the boundary layers by careful use of a thin laser illumination sheet and correct choice of laser pulse separation. Within a boundary layer exhibiting large velocity gradient, the velocity bias was calculated to be small.

ACKNOWLEDGEMENTS

The authors wish to thank the following people at Loughborough University of Technology for their help with this work: Dr. W. M. Malalasekera and Henk Versteeg for their guidance with the numerical model and Steve Taylor and Mark Thompson for building the experimental rig. We also gratefully acknowledge the Chinese State Education Commission and the British Council for sponsoring the first author.

APPENDIX: NOMENCLATURE

$a_p\phi_p$	calculated values at node p
$a_k\phi_k$	calculated values surrounding node p
B_f	fractional bias
d	disc radial–tip clearance
d_I	interrogation region size
h	height of disc chamber
G	aspect ratio of disc chamber, h/R_d
K	ratio of angular velocities of fluid core and rotating disc, β/Ω
M	camera magnification
p	fluid pressure
$\bar{R}$	normalized residual
R_d	radius of disc
Re	disc rotational Reynolds number based on disc outer radius, $\Omega R_d^2/\nu$
α	underrelaxation factor
β	angular velocity of fluid core
μ	dynamic viscosity of fluid
ν	kinematic viscosity of fluid
ρ	density of fluid
Ω	angular velocity of rotating disc
Δt	pulse separation of laser sheet
Δu	maximum excursion of velocity from mean within interrogation cell
Δz	laser sheet thickness
$\mathrm{d}u/\mathrm{d}z$	velocity gradient across light sheet thickness
r, θ, z	cylindrical co-ordinate system
u, v, w	radial, circumferential and axial velocity components.

REFERENCES

1. J. W. Daily and R. E. Nece, 'Chamber dimension effects on induced flow and frictional resistance of enclosed rotating disks', *ASME J. Basic Eng.*, **82**, 217 (1960).
2. Y. Nakata, J. Y. Murthy and D. E. Metzger, 'Computation of laminar flow and heat transfer over an enclosed rotating disk with and without jet impingement,; *ASME J. Turbomach.*, **114**, 881 (1992).

3. J. W. Chew, 'Development of a computer program for the prediction of flow and heat transfer in a rotating cavity', *Int. j. numer methods fluids*, **4**, 667 (1984).
4. P. Bar-Yoseph, J. J. Blech and A. Solan, 'Finite element solution of the Navier–Stokes equations in rotating flow', *Int. j. numer. methods eng.*, **17**, 1123 (1981).
5. D. Dijkstra and G. J. F. Van Heijst, 'The flow between two finite rotating disks enclosed by a cylinder', *J. Fluid Mech.*, **128**, 123 (1983).
6. A. S. Sambo, 'Numerical computation of laminar flows in rotor-stator cavities,' *Proc. 4th Int. Conf. on Numerical Methods in Laminar and Turbulent Flow*, Pineridge, Swansea, 1985, p. 274.
7. J. W. Chew, 'Numerical prediction for the flow induced by an enclosed rotating disc,' *ASME Paper 88-GT-127*, 1988.
8. A. Riahi and P. G. Hill, 'Turbulent swirling flow in short cylinder chambers,' *ASME J. Fluids Eng.*, **115**, 444 (1993).
9. *FLUENT Version 3.02 User Manual*, Vols 1 and 2, Creare Inc., Hanover, USA, 1990.
10. C. J. D. Pickering and N. A. Halliwell, 'Speckle photography in fluid flows: signal recovery with two-step processing', *Appl. Opt.*, **23**, 1128 (1984).
11. R. J. Adrian, 'Scattering particle characteristics and their effect on pulsed laser measurement of fluid flow: speckle velocimetry vs. particle image velocimetry', *Appl. Opt.*, **23**, 1690 (1984).
12. R. J. Adrian, 'The role of particle image velocimetry in fluid mechanics', *Proc. Optical Methods and Data Processing in Heat and Fluid Flow*, IMechE, p. 1, London, April 1992.
13. S. V. Patankar, *Numerical Heat Transfer and Fluid Flow*, McGraw-Hill, New York, 1980.
14. *VISIFLOW—2D Flow Analysis System Manual*, AEA Technology, Harwell, UK, 1992.
15. R. D. Keane and R. J. Adrian, 'Optimisation of particle image velocimeters. Part 1: Double pulsed system,' *Meas. Sci. Technol.*, **1**, 1202 (1990).
16. D. L. Reuss, R. J. Adrian, C. C. Landreth, D. T. French and T. D. Fransler, 'Instantaneous planar measurements of velocity and large-scale vorticity and strain-rate in an engine using particle image velocimetry', *SAE Paper 890616*, 1989.
17. C. Gray, 'The evolution of particle image velocimetry', *Proc. Optical Methods and Data Processing in Heat and Fluid Flow*, IMechE, p. 19, London, April 1992.